

UCSF

UC San Francisco Previously Published Works

Title

Spatial mapping reveals granuloma diversity and histopathological superstructure in human tuberculosis.

Permalink

<https://escholarship.org/uc/item/5p71p9vj>

Journal

Journal of Experimental Medicine, 220(6)

Authors

Sawyer, Andrew
Patrick, Ellis
Edwards, Jarem
[et al.](#)

Publication Date

2023-06-05













DOI

10.1084/jem.20221392

Peer reviewed

TECHNICAL ADVANCES AND RESOURCES

Spatial mapping reveals granuloma diversity and histopathological superstructure in human tuberculosis

Andrew J. Sawyer^{1,2,3} , Ellis Patrick^{4,5,6} , Jarem Edwards^{1,7} , James S. Wilmott^{1,3,7} , Timothy Fielder⁸ , Qianting Yang⁹ , Daniel L. Barber¹⁰ , Joel D. Ernst¹¹ , Warwick J. Britton^{2,12} , Umaimainthan Palendira^{1,2,3} , Xinchun Chen¹³ , and Carl G. Feng^{1,2,3,14} 

The hallmark of tuberculosis (TB) is the formation of immune cell-enriched aggregates called granulomas. While granulomas are pathologically diverse, their tissue-wide heterogeneity has not been spatially resolved at the single-cell level in human tissues. By spatially mapping individual immune cells in every lesion across entire tissue sections, we report that in addition to necrotizing granulomas, the human TB lung contains abundant non-necrotizing leukocyte aggregates surrounding areas of necrotizing tissue. These cellular lesions were more diverse in composition than necrotizing lesions and could be stratified into four general classes based on cellular composition and spatial distribution of B cells and macrophages. The cellular composition of non-necrotizing structures also correlates with their proximity to necrotizing lesions, indicating these are foci of distinct immune reactions adjacent to necrotizing granulomas. Together, we show that during TB, diseased lung tissue develops a histopathological superstructure comprising at least four different types of non-necrotizing cellular aggregates organized as satellites of necrotizing granulomas.

Introduction

Tuberculosis (TB) remains a major cause of mortality, with 1.5 million deaths in 2020 (World Health Organization, 2021). Development of new TB vaccines and therapeutics remains a global priority and depends on a deep understanding of mechanisms mediating resistance to *Mycobacterium tuberculosis* (M.tb), the causative agent of TB (O’Garra et al., 2013; Orme et al., 2015; Libardo et al., 2018). The battle between the host and the pathogen occurs at the level of immune cell-enriched lesions called granulomas (Ramakrishnan, 2012). While being recognized as protective structures for walling-off infection, granulomas also contribute to the survival of mycobacteria and, importantly, are the major manifestation of lung damage (Hunter, 2016; Hunter, 2011; Cohen et al., 2022; Lin et al., 2014).

Despite the critical role of granulomas in host defense, the cellular basis of the TB granuloma formation is incompletely

defined. Investigations of granulomas in human tissues are hampered by the lack of access to clinical samples and limited imaging technologies. In addition, commonly used laboratory mouse strains do not form lesions with the key features of human granulomas (Barry et al., 2009; Williams and Orme, 2016; Basaraba and Hunter, 2017). These hurdles are further compounded by the challenges in granuloma classification due to the high variation in lesion size and histopathological features in diseased human tissues (Welsh et al., 2011; Cadena et al., 2017). Consequently, most studies choose to characterize one or two types of lesions (e.g., non-necrotizing and necrotizing) in isolation. The extent of variation in cellular composition and organization across TB lesions in human lungs has not been characterized using contemporary tools, such as immunostaining and computer-guided quantitative image analysis.

¹School of Medical Sciences, Faculty of Medicine and Health, The University of Sydney, Sydney, Australia; ²Centenary Institute, The University of Sydney, Sydney, Australia; ³Charles Perkins Centre, The University of Sydney, Sydney, Australia; ⁴School of Mathematics and Statistics, Faculty of Science, The University of Sydney, Sydney, Australia; ⁵Centre for Cancer Research, Westmead Institute for Medical Research, The University of Sydney, Westmead, Australia; ⁶Sydney Precision Data Science Centre, The University of Sydney, Sydney, Australia; ⁷Melanoma Institute Australia, The University of Sydney, Sydney, Australia; ⁸Department of Tissue Pathology and Diagnostic Oncology, Royal Prince Alfred Hospital, Camperdown, Australia; ⁹Guangdong Key Lab for Diagnosis and Treatment of Emerging Infectious Diseases, Shenzhen, Third People’s Hospital, Shenzhen, Shenzhen, China; ¹⁰Laboratory of Parasitic Diseases, National Institute of Allergy and Infectious Diseases, National Institutes of Health, Bethesda, MD, USA; ¹¹Division of Experimental Medicine, Department of Medicine, University of California San Francisco, San Francisco, CA, USA; ¹²Department of Clinical Immunology, Royal Prince Alfred Hospital, Camperdown, Australia; ¹³Guangdong Key Laboratory of Regional Immunity and Diseases, Department of Pathogen Biology, Shenzhen University School of Medicine, Shenzhen, China; ¹⁴Institute for Infectious Diseases, The University of Sydney, Sydney, Australia.

Correspondence to Carl G Feng: carl.feng@sydney.edu.au; Xinchun Chen: chenxinchun@szu.edu.cn.

© 2023 Sawyer et al. This article is distributed under the terms of an Attribution–Noncommercial–Share Alike–No Mirror Sites license for the first six months after the publication date (see <http://www.rupress.org/terms/>). After six months it is available under a Creative Commons License (Attribution–Noncommercial–Share Alike 4.0 International license, as described at <https://creativecommons.org/licenses/by-nc-sa/4.0/>).

Recent advancements in spatial transcriptomics and proteomics technologies enable researchers to image mycobacterium-infected tissues at various levels. Spatial transcriptomics have provided comprehensive gene expression information across tissue sections of human leprosy (Ma et al., 2021) and murine TB (Carow et al., 2019), although the current technologies do not have the resolution required for single-cell imaging. Antibody-based multiplexed imaging approaches (Abengozar-Muela et al., 2020; McCaffrey et al., 2022), including one with multiplexed ion beam imaging by time of flight (MIBI-TOF), have been employed to examine human TB granulomas with single-cell resolution. The MIBI-TOF study has successfully revealed diverse microenvironments within human TB granulomas (McCaffrey et al., 2022). However, this approach interrogates selected regions of individual lesions, and its scope in tissue-wide cross-lesion comparative analysis is limited (Tan et al., 2020; Hartmann and Bendall, 2020). Because only a subset of lesions was analyzed, it is unclear whether the observed difference in microenvironments reflects the cellular structural variations within a lesion or across multiple lesions. Therefore, revealing the level of granuloma diversity by analyzing many lesions across large areas of diseased tissue will deepen the understanding of these intra-lesion microenvironments.

To capture all cellular structures in TB lung samples, we have employed multiplex Opal immunofluorescence (IF) to map the tissue-wide immune landscape with single-cell resolution (size ranging from 100 to 300 μm^2). We also developed a granuloma identification and classification strategy to minimize the bias commonly associated with lesion analysis. By spatially mapping individual immune cells across all lesions in each sample (13 TB patients in total), representing 726 lesions (defined as distinct immune cell aggregates) across all patients with ~ 9 million total cells, we established that human TB lung tissues contain, in addition to well-recognized necrotizing lesions, at least four types of compositionally and spatially distinct non-necrotizing lesions. The latter lesion structures were shaped by the neighboring necrotizing granuloma as well as by intra-lesion organization of immune cells, suggesting that granuloma architecture is governed by lesion-intrinsic and -extrinsic signals in human TB.

Results

Active pulmonary TB is associated with extensive tissue consolidation and development of immune cell aggregates in the lungs

To gain information on a tissue-wide inflammatory response to *M.tb* in human lungs, we first examined hematoxylin and eosin (H&E)-stained tissues from 13 patients who underwent partial lung resection due to unsuccessful antibiotic therapy (Fig. S1 A). In contrast to healthy lungs with clear alveolar space, the landscape of diseased tissues was highly complex with regions of consolidation and foci of leukocytes (Fig. 1 A). The well-recognized necrotizing granulomas were frequently accompanied by many non-necrotizing granulomas and lymphoid aggregates (Fig. 1, A and B). This superstructure was consistently observed across all but one patient sample, representing a common histopathological landscape in the lungs of active TB

patients (Fig. 1 C). The areas surrounding the foci are composed of infiltrating leukocytes and fibroblast-like cells, which may represent stages of TB disease distinct from that associated with cellular aggregates.

To visualize the immune landscape across entire lung sections, tissues were stained with the major immune lineage markers CD68 (macrophages), CD20 (B cells), CD8 (CD8⁺ T cells), and CD4 (CD4⁺ T cells), together with nuclear dye DAPI (Fig. 1 D). High-resolution 20 \times regional images were stitched digitally to reconstruct images of the entire plane of a tissue section, allowing for visualization of each tissue section in its entirety and at a single-cell resolution. We observed extensive infiltration of immune cells across all tissue sections, which was mirrored in the H&E-stained sections from the same patient. Giant cells were observed across patients and proliferative (Ki-67⁺) cell aggregates were observed in two patients (Fig. S1, B and C).

To assess whether the diverse structures defined pathologically could be captured and analyzed at a single-cell level, we first examined DAPI staining on lung sections. To objectively distinguish healthy lung tissue from consolidated areas and cellular aggregates in the IF images, healthy and inflamed regions were first stratified based on the relative density of nucleated cells on the Opal IHC image, following cell segmentation with DAPI (Fig. S1 D). The variations in the density across TB tissues were visualized with 3D projection (Fig. 1 E), where the height of the peaks (z-axis) indicates cell density. Each distinct peak represents a cell aggregate and a trough (colored in white) reports an acellular necrotizing lesion.

The positivity threshold for each region was determined as described in the methods. Briefly, based on distinct cell density values in different regions (defined based on the images of matching H&E-stained sections; Fig. S1 E), cellular aggregates (CA) were identified as areas with densities between 50 and 100% of the maximum density, consolidated tissues (CT) between 25 and 50%, and healthy lung tissue as below 25%. When mapped back onto the tissue, the localization of the cell density-defined regions matched closely to the regions identified on H&E-stained sections (Fig. 1, A and F).

Next, we compared the composition of major immune cell populations in the consolidated region and cellular aggregates and found that, as a proportion of total DAPI⁺ cells, CD68⁺, CD8⁺, CD20⁺, and CD4⁺ cells were all significantly more abundant in the cellular aggregates compared to the consolidated region (Fig. 1 G). These observations indicate that these immune cell-enriched cellular aggregates, defined by our computer-guided cell density-based method, are distinct lesions within the consolidated region and resemble the “granulomas” and lymphoid aggregates defined conventionally with histopathological features. To define immune cell aggregates more precisely, we refined our lesion identification strategy by performing kernel density analysis and lesion definition only on cells stained positively for immune markers (Fig. 1 H). In the remainder of this investigation, we have employed this computer-guided method to define individual immune cell aggregates in human tissues. We have focused our analysis on cellular aggregates containing 20–100% of the maximum immune cell density per patient, which included 726 lesions, including 20 structures containing a

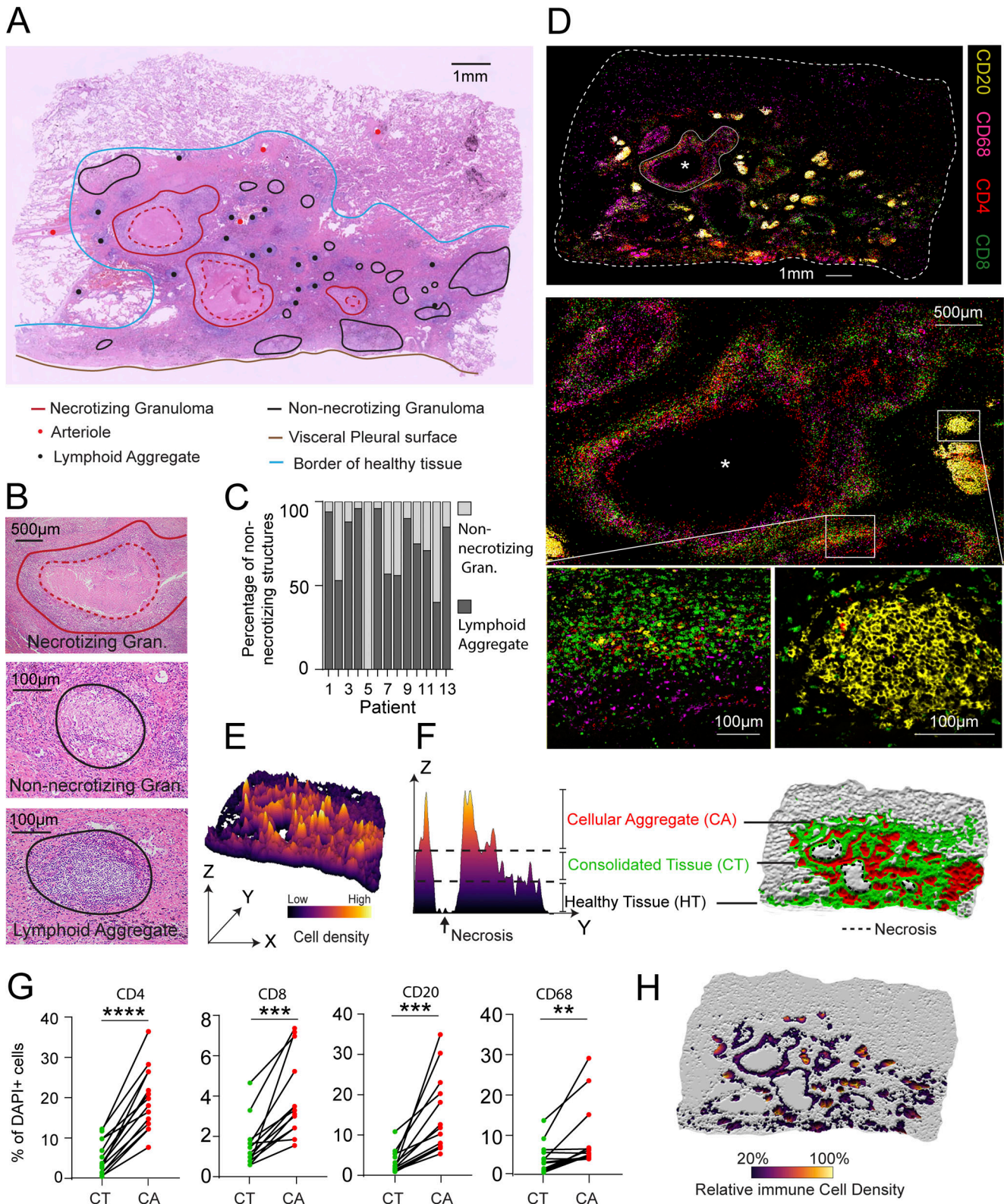


Figure 1. **Active pulmonary TB is characterized by development of histopathological superstructures in the lung.** (A) A TB lung tissue section stained with H&E with various histological and histopathological features indicated. (B) Enlarged example images of distinct lesion types identified in A. The outer and inner borders of necrotizing lesions were marked with solid and dotted red lines, respectively. The borders of non-necrotizing lesions were marked with solid black lines. (C) The proportion of non-necrotizing granulomas and lymphoid aggregates across 10 patients. Each color represents one type of non-necrotizing structure. (D) Composite Opal IF image of the same tissue section in A stained for major immune populations inlaid with magnified views of a necrotizing lesion (top panel, circled by a white line, *necrotizing core) and two non-necrotizing regions (bottom panel, rectangle boxes). (E) 3D diagram showing the variations in the density of DAPI⁺ segmented cells across entire TB lung section from A. The height of the peak (z axis) indicates cell density. (F) A representative 2D

histogram showing a cross-section (indicated by the white dotted line in C) along y and z axis. The three z-axis segments (divided by dotted lines) are defined based on cell density and correspond to the regions of healthy, consolidated tissue and cellular aggregates shown in the pseudo-color topography image (right) of the same TB lung tissue as in A and C. Dotted lines indicate boundaries of necrotic areas. **(G)** Percentage of major immune cell populations among total DAPI-positive cells in CT (green) versus CA region (red). Each paired point represents a patient. The level of statistical significance is determined using a Wilcoxon signed-rank test and a P value <0.05 was considered statistically significant. *P < 0.05; **P < 0.01. **(H)** Distribution of immune cell-containing cell aggregates (colored) across the same tissue section as in A. The lesions selected are high in cellularity and positive for at least one of four major immune cell lineage markers (CD4, CD20, CD8, or CD68). Color intensity of non-greyed areas correlates inversely with immune cell density of the region relative to the maximum density in the tissue.

central necrotizing cavity, across 13 patients. Together, this lesion identification approach has revealed previously unappreciated complexity in the cellular landscape of human TB granulomas.

Cellular aggregates are highly diverse and fall across a continuous spectrum underpinned by the density of CD20⁺ cells

Opal images revealed that the immune cell compositions in TB lesions are highly diverse (Fig. 2 A). To quantify this lesion heterogeneity, we analyzed the density of each immune cell type across 726 lesions from 13 patients. For necrotizing lesions, the central area of necrosis was excluded to optimize comparison with non-necrotizing lesions. The density of individual immune cell populations varied significantly across lesions (up to three logs). The variation was more apparent in non-necrotizing lesions than in their necrotizing counterparts (Fig. 2 B). CD20⁺ B cells and CD4⁺ T cells were more abundant in non-necrotizing lesions while CD68⁺ macrophages were more abundant in necrotizing lesions. CD8⁺ T cells distributed indistinguishably between necrotizing and non-necrotizing lesions.

To assess whether lesions cluster into distinct groups based on their immune cell composition, we performed principal component analysis (PCA) on all lesions based on the density of four major immune cell populations. We did not observe clustering of lesions into distinct groups, although necrotizing lesions (colored in red) tend to cluster closely (Fig. 2 C), indicating a continuous spectrum of lesion compositions. PC1 represented the largest share of variation (38.3%) and this continuous spectrum of the lesions is underlined mainly by the variations in CD20⁺ B cell density. While the lack of clustering using major lineage markers likely represents a biological spectrum in granuloma composition, the use of highly multiplex staining with more markers in future studies may clarify if additional lesion subtypes could be identified. There appeared to be low inter-patient variation except for one patient with an increased density of CD8⁺ T cell (Fig. 2 D). This patient (Patient 2) underwent lung resection prior to anti-M.tb therapy, and it is unclear if drug treatment influenced CD8⁺ T cell abundance.

Lesions can be stratified based on immune cell composition and spatial organization

Having established a spectrum of lesion compositions based on immune cell density, we next determined whether lesions have a diverse spatial arrangement of cells. As expected, necrotizing lesions were characterized by their acellular central core (Fig. 3 A). However, within non-necrotizing solid lesions, cells were also found to distribute unevenly, and in some lesions most of

the cells preferentially localized in the central region whilst in others most cells localized peripherally leaving a loose but non-necrotizing central area. To analyze this spatial variation, we devised a “total cell central preference index (tCPI)” to give a single number readout of whether a lesion tends to have an increased or reduced cellular density in its central area compared to the average density of the lesion (Fig. 3, B and C). Briefly, the metric works by measuring the distance of all cells from the lesion’s outer border and then dividing cells into an inner 50% of cells and an outer 50% of cells. The area covered by the outer 50% of cells is divided by the total lesion area to give an output of <0.5 if there is a reduced density of cells in the central area of the lesion. When the tCPI was compared between necrotizing and non-necrotizing lesions, the former lesions had significantly lower central preference index than non-necrotizing lesions (Fig. 3 D), validating the approach in quantifying cell spatial distribution in granulomas.

We next investigated if the cell density and tendencies of immune cells to locate toward or away from the lesion center could facilitate lesion stratification. We performed a pairwise comparison of PC1 (driven mainly by B cells) from the previous PCA (Fig. 2 C) and central preference index measurement. We termed this lesion identification and classification algorithm as LANDSCAPE (lesion and neighbourhood description stratified by cellular composition and position estimates). In addition to necrotizing lesions readily identifiable on H&E-stained sections, this analysis revealed four types of solid lesions (Fig. 3 E). All four lesion types were identified in all but one patient analyzed although there were variations in the proportion of each lesion type across patients (Fig. 3 F and Fig. S2 A), suggesting that the lesion types identified represent common immune features of the local tissue response in human TB lungs.

The cellular characteristics of the lesion types defined using LANDSCAPE analysis were consistent with those presented on multiplexed IF images of the same lesion type (Fig. 3, E and G). Type I and II lesions have a high density of B cells but differ in cellular organization around the lesion center (high vs. low tCPI; Fig. S2, B–D). Type III and IV lesions had reduced B cell density and increased macrophages and also varied in cellular organization around the lesion center (high vs. low tCPI). These descriptions were reinforced by the finding that all necrotizing/cavitary lesions fell into the type IV quadrant (Fig. 3 E, lesions shown in the box area).

Divergent intra-lesion spatial distribution of CD20⁺ cells and CD68⁺ cells determine the types of non-necrotizing granulomas

To understand the relationship between the spatial distribution of individual immune cell populations and granuloma types, we

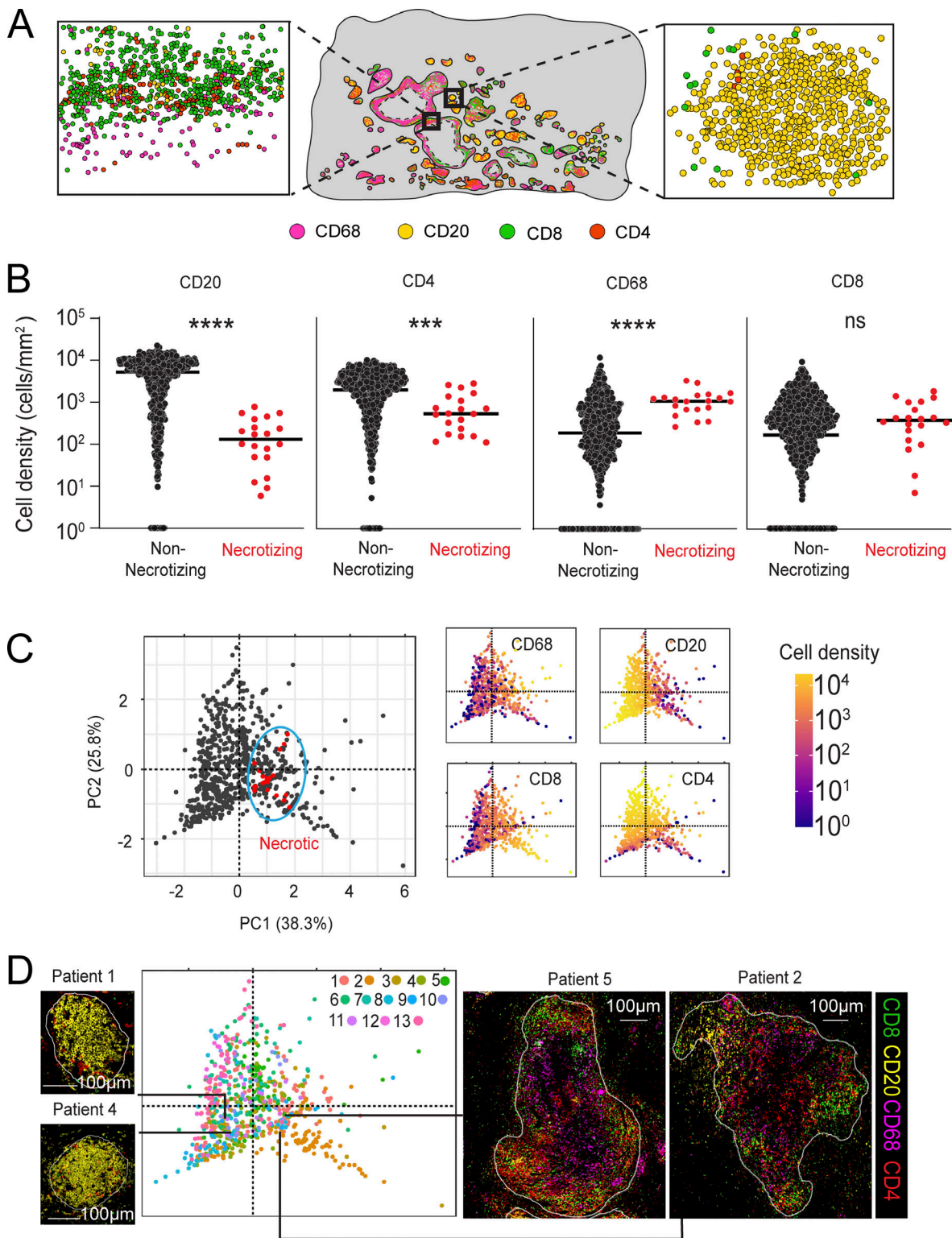


Figure 2. Lesions have diverse compositions but fall across a continuous spectrum underpinned by CD20⁺ cell density. (A) Image of segmented immune cells in positively identified lesions in TB lung from Fig. 1 A with two representative areas (boxed) showing distinct cellular composition. (B) The density of each major immune cell population in necrotizing and non-necrotizing lesions from 13 patients. Each symbol represents an individual lesion and lines indicate group median. The level of statistical significance is determined using a Mann-Whitney test and a P value <0.05 was considered statistically significant. ****P < 0.0001; ***P < 0.001. (C) PCA plot of all lesions (n = 726) with necrotizing lesions indicated in red and circled by an ellipse. Additional marker-specific PCA plots are colored according to the density of marker-positive cells. (D) PCA plot visualization of all lesions across 10 patients. Each color indicates one patient, and each symbol represents an individual lesion. Images of example lesions of four individual patients are shown.

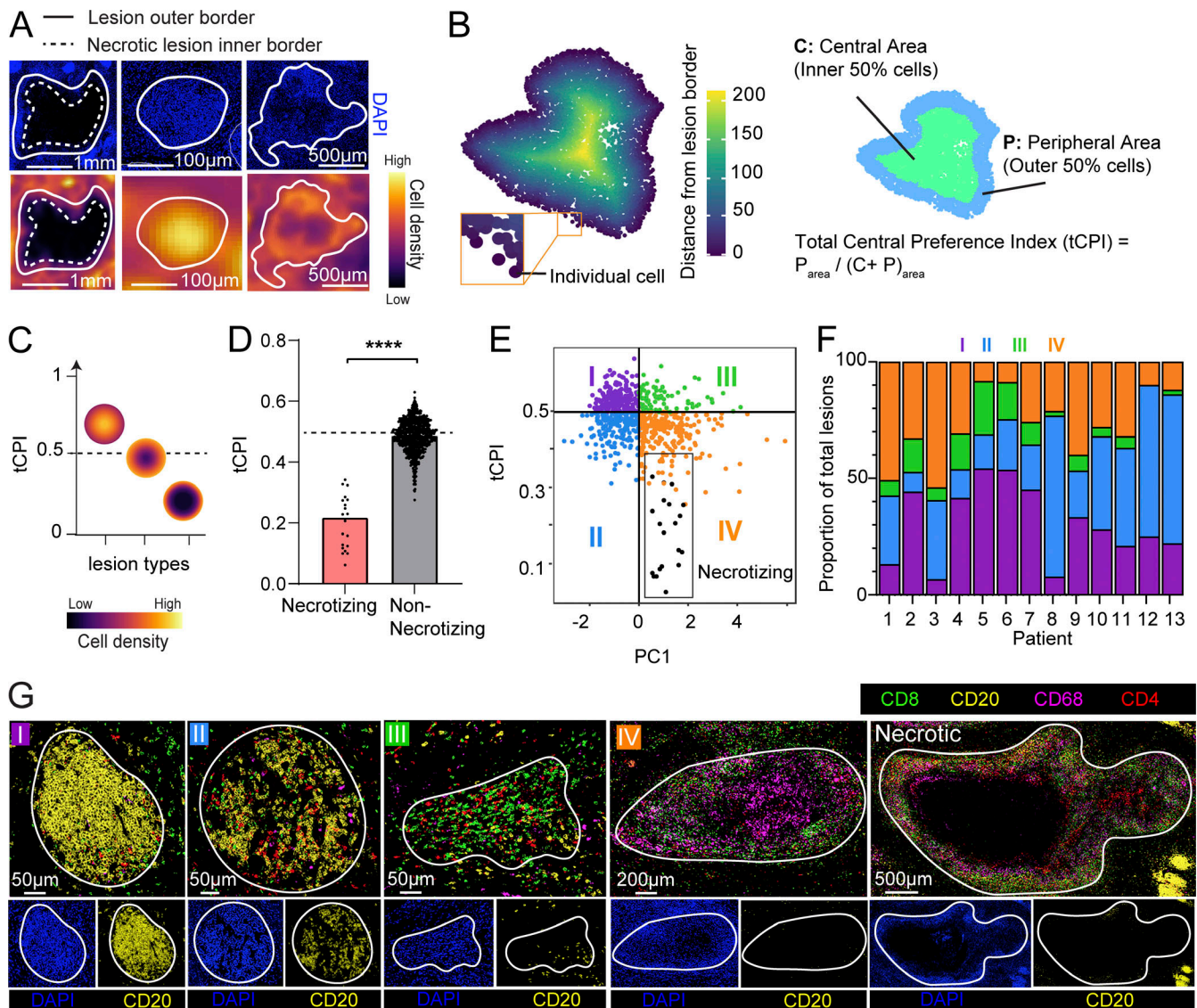


Figure 3. Combined analysis of compositional and spatial features identifies four types of TB lesions. (A) Top: Images of DAPI-stained tissue showing variations in intra-lesion cell distribution. Bottom: Heatmap images showing the same three lesions with relative cell density indicated. (B) Left: A lesion image with the distance of each individual cell from the lesion border indicated by color density. Right: The same lesion with areas colored according to which cells are closer or further from the lesion border relative to the median distance. The equation used to calculate total cell central preference index is shown. (C) Schematic diagram illustrating the intra-lesion cell distribution patterns and their corresponding tCPI. (D) tCPI compared between necrotizing and non-necrotizing lesions. Each symbol represents an individual lesion. Bars indicate the group median. The level of statistical significance is determined using a Mann–Whitney test, **** $P < 0.001$. (E) Pairwise comparison of PC1 from Fig. 2 C against tCPI. Each symbol represents an individual lesion. Lesions ($n = 726$) are divided into four subpopulations with the quadrants being set at $PC1 = 0$ and $tCPI = 0.5$. The fifth type of lesions, necrotizing lesions (black symbols), are additionally indicated in the boxed area. (F) Proportion of each lesion type across 10 patients. Each color represents one lesion type. (G) Representative multiplex images of each lesion type with correlated images of DAPI and CD20 staining are shown below each multiplex image.

quantified the relative distance of lymphoid cells and macrophages from the lesion border and termed the measurement as “immune cell central preference index” (immCPI; Fig. 4, A and B). We found that CD20⁺ cells were located more peripherally in type IV lesions compared to types I, II, and III, while CD68⁺ cells were located more centrally in type IV lesions compared with the other three types of solid lesions (Fig. 4 C). These data highlight further cellular structural differences between lesion types and suggest a progression of CD20 and CD68 cell localization between lesion types.

CD14⁺ CD68⁺ monocyte/macrophage populations preferentially localize at the necrotizing border

Necrotizing granulomas are formed when a host fails to contain *M.tb* replication or regulate the local inflammatory response (Pagán and Ramakrishnan, 2018). However, there is limited knowledge of how the infection niche is walled off and how immune cells are spatially organized at the border of necrotizing (acellular) regions. We co-stained sections with antibodies against purified protein derivative (PPD) of *M.tb* to determine the localization of infection foci in lung sections. *M.tb* was

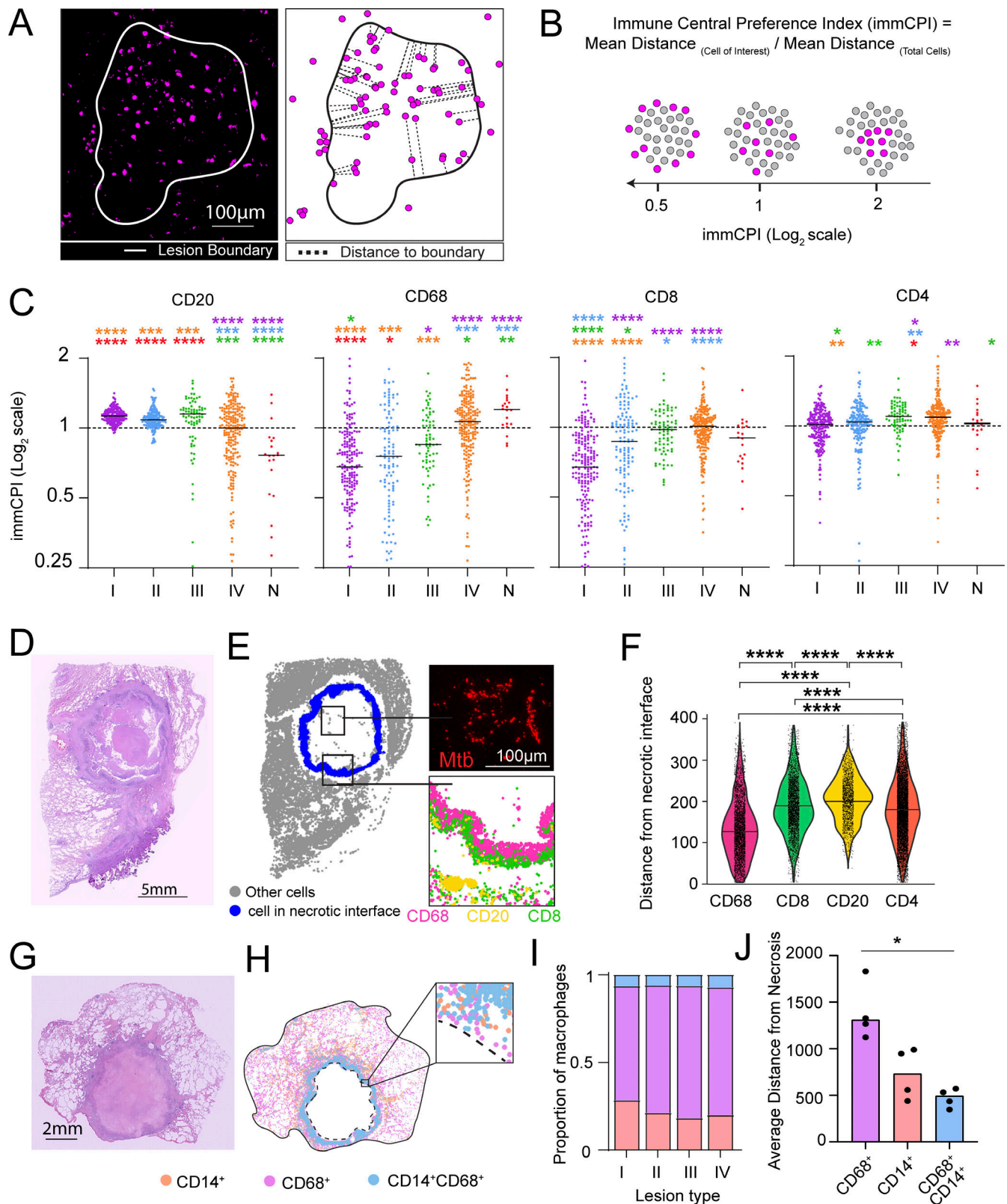


Figure 4. **Spatial organization of CD68⁺ macrophages is lesion-type dependent.** (A) A lesion image with CD68 staining (left) and a diagram illustrating the measurement of the closest distance of individual CD68⁺ cells from the lesion border (right). (B) The formula for calculating the spatial distribution of a cell-of-interest within a lesion. Schematic diagram of the lesions with representative immCPI measurements. (C) immCPI of each immune cell type across lesion type. Each symbol represents an individual lesion. Solid lines indicate group median and dashed lines indicate an immCPI of 1. (D) Image of a H&E-stained TB lung sample. (E) Pseudo-color image of the section from D with the necrotizing border indicated in blue. The magnified images of the boxed areas show positive M.tb staining and spatial position of CD68⁺, CD20⁺, and CD8⁺ cells. (F) Distance of individual immune cell population from necrotizing border in a

representative lesion. Each symbol represents an individual cell and lines indicate group median. **(G)** Image of a H&E-stained TB lung sample. **(H)** Spatial distribution of monocyte/macrophage populations defined by CD14 and CD68 in tissue section from G, with the magnified image showing individual segmented myeloid cells. **(I)** Proportion of each macrophage subset by lesion type. **(J)** Distance of each macrophage subset from the closest necrotizing area across the entire tissue section. Each symbol represents an individual patient and column height indicates the group median. The level of statistical significance in C, F, and J is determined using a Kruskal–Wallis test with Dunn’s multiple comparisons test and an adjusted P value <0.05 was considered statistically significant. *P < 0.05; **P < 0.01; ***P < 0.001; ****P < 0.0001.

identified exclusively in the necrotizing region in the sections analyzed (Fig. 4, D and E; and Fig. S2, E and F), consistent with previous studies (Hunter et al., 2014; Urbanowski et al., 2020), though differing from a recent study that identified M.tb in non-necrotizing lesions when an anti-BCG antibody was used (Ulrichs et al., 2004). Although Ki-67⁺ cells have been identified in necrotizing lesions previously (Ulrichs et al., 2004), our analysis quantitatively established that Ki-67⁺ cells are preferentially localized in necrotizing over non-necrotizing lesions (Fig. S2 G). To map the cellular microenvironment of the necrotizing border, we measured the distance of each immune cell in necrotizing lesions from the necrotizing interface and found that CD68⁺ cells were localized closest to the necrotizing core as shown previously (Tsai et al., 2006), followed by CD8⁺ and CD20⁺ cells (Fig. 4 F and Fig. S2 H).

We next stained a subset of patient samples ($n = 5$) for CD14 to better understand macrophages/monocyte populations in TB lesions (Fig. 4, G and H). The relative abundance of CD14⁺ CD68⁻, CD14⁻ CD68⁺, and CD14⁺ CD68⁺ subsets was comparable across all four types of granulomas (Fig. 4 I). However, while at the whole tissue level, CD14⁺ CD68⁺ cells represented the least abundant subset relative to the other two populations, they localized significantly closer to the necrotizing core (Fig. 4 J), revealing a previously unrecognized spatial distribution of different myeloid cell populations at the necrotizing interface.

The distance to necrotizing lesions correlates with the relative abundance of specific immune cell populations in the surrounding non-necrotizing lesions

Our analysis revealed that necrotizing lesions are surrounded by diverse solid lesions (Fig. 1 A and Fig. 5 A), which raises questions about the spatial relationship between necrotizing and various non-necrotizing lesions. To determine the inter-lesion relationships, we measured the minimum distance from each lesion to every other lesion on the same tissue section (Fig. 5 B). Given the cellular organization we observed around necrosis, we compared the distance of lesions of each type to the closest necrotizing lesion. We found that lesions of type I and II tend to be twice as close to a necrotizing lesion as lesions of type III and IV (Fig. 5 C).

To explore the correlation of lesion distance from necrotizing lesions to lesion composition, we divided lesions of each type into those localized >500 μm from necrotizing lesions and those <500 μm . We found that the lesions of type I and IV had more CD4⁺ cells when they localized closer to necrotizing lesions (<500 μm) compared with those further away from necrosis (>500 μm ; Fig. 5 D). Type II and III lesions contain more CD20⁺ cells when they were closer than 500 μm compared to when they were further. There was no difference in the density of

CD8⁺ or CD68⁺ cells in any lesion type when comparing the distance of the lesions from the closest necrotizing lesion (Fig. S2 I). These results suggest that potential crosstalk between necrotizing and certain types of non-necrotizing lesions contribute to the formation of multi-lesion superstructures in the lung.

Formation of non-necrotizing lesions is shaped by the proximity to necrotizing granulomas and intra-lesion organization of CD20⁺ and CD68⁺ cells

Since granulomas are diverse, lesion–lesion interactions may also play a role in regulating lesion progression and overall lung pathology. We combined both compositional and spatial measurements and performed trajectory analysis on all lesions. Lesion progression correlated with the order of the four types of lesions, and necrotizing lesions consistently fell at one end of a spectrum (Fig. 5, E and F). CD20⁺ cell density, as well as the central preference of total leukocytes, CD20⁺, and CD68⁺ cells all follow along the progression trajectory closely. This suggests that the lesion types included in this analysis may represent distinct yet related stages of granuloma maturation, from B cell-enriched lymphocytic foci to macrophage-centered granulomas, and some of the latter lesions may eventually develop into necrotizing tissue whereas others become healed or fibrotic lesions (Fig. 5 G). Similarly, type I lesions may contain both distinct tertiary lymphoid structures (TLS) and B cell-enriched infection foci. In this study, only the well-formed cellular aggregates were included in the trajectory analysis, and our samples were collected at a later stage of active TB disease. Therefore, our analysis considers neither the large consolidated inflammatory regions nor other early cellular events preceding the formation of type I lesions. These early events could include yet defined type(s) of solid granulomas and/or development of pneumonia as suggested previously by Medlar that granulomas originate from microscopic foci of pneumonia in the lungs of TB patients (Medlar, 1948). Future high-dimensional phenotyping of samples with different clinical outcomes will assist in defining early cellular events and branchpoints along the lesion progression.

Discussion

Recent work in M.tb-infected non-human primates and patients has revealed that TB lesions are heterogenous in their histopathological features (Subbian et al., 2015; Abengozar-Muela et al., 2020; Wells et al., 2021), metabolic activities (Kim et al., 2010; Mattila et al., 2017), inflammatory signaling (Marakalala et al., 2016; Cronan et al., 2021), and pathogen burdens (Gideon et al., 2022; Lin et al., 2014; Martin et al., 2017). Collectively, these studies indicate that TB represents a spectrum of clinical

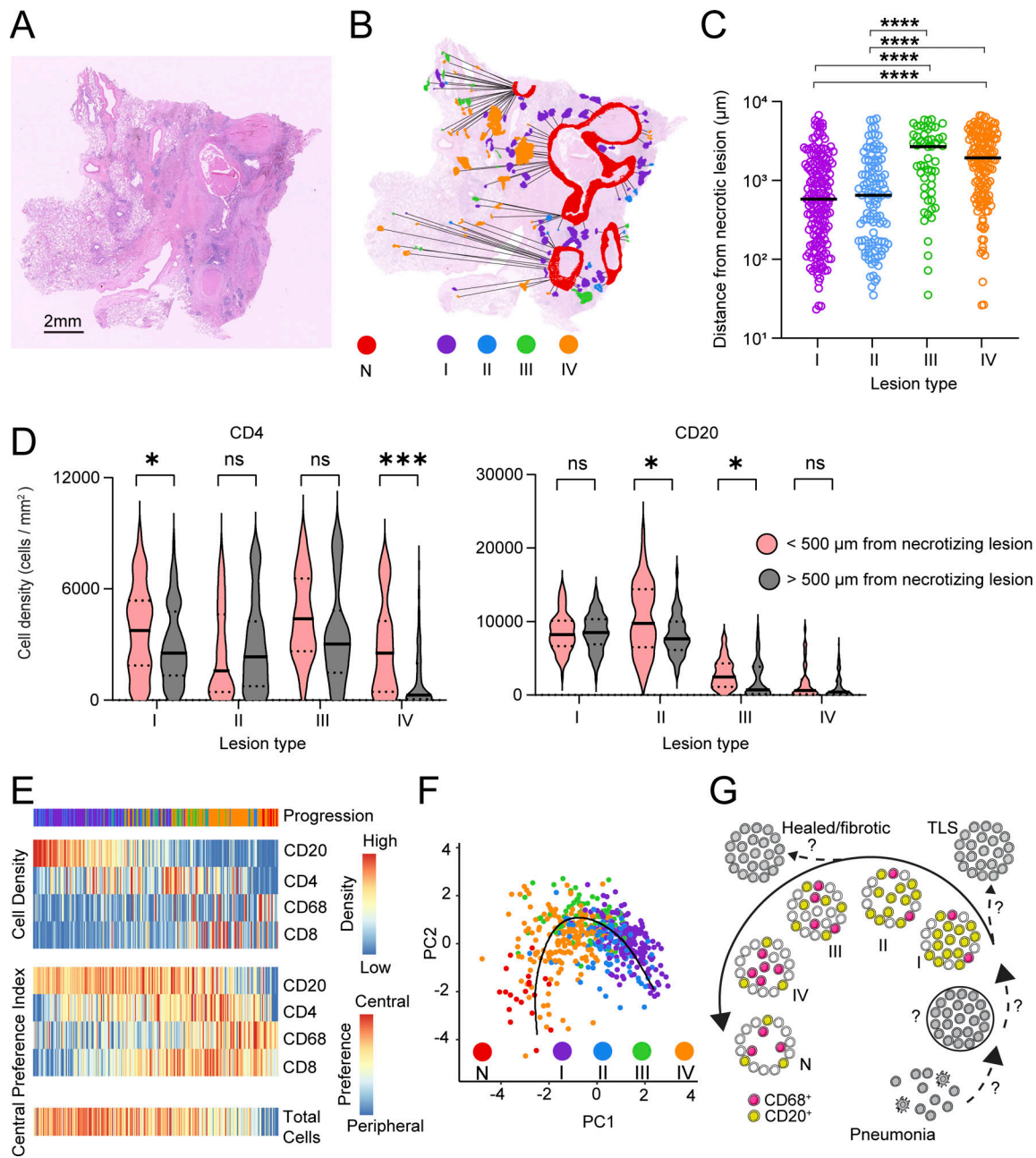


Figure 5. Formation of non-necrotizing lesions is shaped by the neighboring necrotizing granuloma and intra-lesion organization of CD20⁺ and CD68⁺ cells. (A) Image of a H&E-stained TB lung sample. (B) The same TB lung section as in A overlaid with the locations of non-necrotizing and necrotizing lesions identified using LANDSCAPE tool. The relationship of each non-necrotizing lesion to the closest necrotizing lesion is indicated with connecting lines. (C) Distance of four types of non-necrotizing lesions to the closest necrotizing granuloma. Each symbol represents an individual non-necrotizing lesion and solid lines indicate the group median. The level of statistical significance is determined using a Kruskal–Wallis test with Dunn’s multiple comparisons test, and an adjusted P value <0.05 was considered statistically significant. ****P < 0.0001; ***P < 0.001; **P < 0.01; *P < 0.05. (D) The density of CD4⁺ and CD20⁺ cells in lesions located greater or less than 500 µm from necrotizing lesions. Solid lines indicate the group median and dotted lines indicate interquartile range. The level of statistical significance is determined using a Mann–Whitney test, and a P value <0.05 was considered statistically significant. **P < 0.01; ***P < 0.001. (E) Heatmap of inter-lesion trajectory analysis based on spatial and compositional parameters of individual lesions defined by LANDSCAPE. Lesions are ranked along the x axis according to trajectory and manually ordered on the y axis. Top panel indicates the lesion type. The analysis was performed using R. (F) Trajectory analysis of all lesions based on spatial and compositional lesion parameters as shown in E. The line indicates inferred trajectory. Each symbol represents an individual lesion (n = 726). (G) Schematic diagram summarizing key findings and illustrating hypothetical lesion progression pathways. Dotted lines indicate hypothetical lesion progression branchpoints and pathways. Question marks represent either lesion types or progression branchpoints yet to be formally determined. Schematic lesions identified in this study are depicted with color whereas those that have yet to be formally determined are shown in grey.

and subclinical manifestations (Barry et al., 2009; Cadena et al., 2017; Lin and Flynn, 2018). By spatially mapping all lesions within each sample, consisting of 726 lesions with a total of over 9 million single cells, we defined four types of non-necrotizing lesions representing a spectrum of distinct yet overlapping cellular architecture. These non-necrotizing lesions, together with necrotizing granulomas, appear to form a histopathological superstructure underlying the immunopathology associated with uncontrolled M.tb infection. Since each lesion type represents a distinct type of immune response and lesions may individually or cooperatively contribute to TB pathogenesis, we suggest that both intra- and inter-lesion analysis should be performed to define the host response to M.tb.

The frequently documented lesions with a necrotizing core represent only one of several types of lesions, suggesting that examination of only one or two stereotypical lesion types is unlikely to capture all the cellular events contributing to the overall lung pathology and clinical outcome. We speculate that the lesion spectrum may reflect the history of ongoing local immune responses to continual seeding of locally disseminated bacteria. Therefore, this heterogenous and dynamic nature captured in each tissue section may be explored to identify distinct cellular structures associated with many if not all the stages of the granuloma maturation process.

The composition and superstructure of lesions formed in humans appear to be different from those reported in C57BL/6 mice (diffuse inflammation without necrosis) or non-human primates (often reported as discrete lesions surrounded by relatively healthy alveolar space). In addition to genetic differences, the discrepancy in the length and frequency of pathogen exposure between infected animals and human subjects may contribute to the variations. In our study, the samples were resected from patients following 3–96 mo of identified lung disease, which contrasts with most animal studies where samples are collected at earlier time points. The prolonged infection in humans contributes to recurring endogenous infection/dissemination, thereby leading to a more complicated and advanced lesion landscape. Moreover, as reviewed by Hunter (2011) and more recently by Urdahl (Cohen et al., 2022), pulmonary TB in adult humans is usually postprimary disease, possibly caused by reinfection, whereas experimentation in animals models correlates to primary TB in humans.

The spatial association between non-necrotizing and necrotizing lesions revealed in this study aligns with previous histological findings (Ulrichs et al., 2004; Cohen et al., 2022; Medlar, 1955; Tsai et al., 2006; Slight et al., 2013) and suggests that these lesions function cooperatively as an inflammatory superstructure to determine the outcome of local immune responses. This observation raises the question of how TB granulomas should be defined at a single-cell level. It is impossible to determine with 2D IF staining whether these structures were structurally connected as has been reported previously with μ CT imaging (Wells et al., 2021). Nevertheless, our results support the hypothesis that the diverse function of granulomas may be reflected in the heterogeneity among granuloma populations (Lin and Flynn, 2018; Gideon et al., 2022).

Our study has several limitations. Firstly, a limited number of samples were examined. Secondly, Opal multiplex technology is only capable of examining small numbers of markers, thereby limiting the depth of cellular analysis. Combining tissue landscape analysis and in-depth region of interest analysis such as MIBI-TOF will lead to an improved understanding of TB lung microenvironments. For example, some of our B cell-enriched type I lesions, which may resemble tertiary lymphoid structures (TLS) formed in mycobacterial infected tissues (Ulrichs et al., 2004), have also been independently identified in the McCaffrey et al. (2022) study. Therefore, it is possible that type I lesions are heterogenous, including conventional TLS and B cell-enriched granulomas. Future deep-phenotyping using high-dimensional imaging technologies will be able to address this question. Finally, since our initial samples were collected due to poor treatment response, whether our study has captured a fraction or the full spectrum of granulomatous lesions remains to be determined. In the future, we will apply our LANDSCAPE strategy to samples from patients with active TB or latent infection in lungs resected for other reasons, which will assist in elucidating the relationship between cellular structure, anti-microbial function, and disease outcomes.

Materials and methods

Patient cohort

We utilized a retrospective cohort of patients from the Shenzhen Third People's Hospital. The study was approved by the Research Ethics Committee of the Shenzhen Third People's Hospital (protocol ID #: 2016-081). All archival specimens were analyzed, with no active participation of human subjects. Active TB diagnosis was based on clinical symptoms, chest radiography, pathological results, microscopy for acid-fast bacilli, M.tb culture, and GeneXpert analysis of sputum (Table S1). Serial sections (5 μ m) of each specimen were stained with H&E and inspected by two clinical pathologists to evaluate the presence of granulomatous inflammation. Patients with comorbid HIV were excluded from the study. All patients with TB were undergoing either anti-TB or other antibiotic therapy.

OPAL staining

Formalin-fixed paraffin-embedded (FFPE) TB lung sections were baked at 65°C for 1 h and dewaxed and rehydrated through gradients of xylene and ethanol. Antigen retrieval was performed by boiling samples to 100°C for 15 min in pH 9 Antigen retrieval buffer (Akoya Biosciences). Tissues were incubated for 45 min at room temperature with primary antibodies specific for CD20 (1:1,000; L26; Cell Marque), CD4 (1:100; SP35; Cell Marque), CD68 (1:500; Kp-1; Cell Marque), CD8 (1:500; ab4055; Abcam), CD14 (1:100; HPA001887; Cell Marque), Ki-67 (1:1,000; D2H10; Cell Signaling Technologies), or PPD (rabbit polyclonal Ab to PPD, Cat# ab905; Abcam). Primary antibodies were detected with OPAL Polymer HRP Ms + Rb (Akoya Biosciences) for 15 min and visualized following a 10-min incubation with Tyramide signal amplification and Opal Fluorophore (Akoya Biosciences) before being boiled at 100°C to strip antibody-HRP complexes from tissue. The process was repeated

until all markers were stained. Following the final marker staining, tissue sections were incubated with DAPI for 10 min and mounted using ProLong Gold (Thermo Fisher Scientific). The images were captured using the Vectra 3.0.5 multispectral imaging system (Akoya Biosciences). A series of high-power $\times 20$ multispectral images (MSIs) covering the entirety of tissue sections were captured.

Cell segmentation

MSIs were unmixed using Inform 2.3 (Akoya Biosciences) and exported as .TIFF images. TIFF images were then imported in HALO3.3.2541.345 (Indica Labs) and digitally stitched to construct single images of entire tissue sections. HALO was trained to segment individual cells based on characteristic nuclear staining in the DAPI channel. To distinguish cell identities, the positivity threshold for each marker was determined, and cell segmentation was performed. Object data (including identity and location information for each cell) for each patient sample was exported, and further analysis was performed in R x64 3.5.3 (R Core Team, 2021).

Density and immune-cell marker-based lesion identification

Kernel density analysis was performed using the “kde2d” function in the MASS (Venables and Ripley, 2002) package in R using a bandwidth of 500 within a 500×500 grid. 3D projections were created with the “persp” function and colored with the “viridis” function from the Viridis package (Garnier et al., 2021). The positivity threshold was determined empirically in a subset of samples by quantifying cell density in the representative areas (defined based on the images of matching H&E-stained sections) within healthy, consolidated, and aggregate regions using HALO. We found that the cell density of three tissue regions varied markedly but the differences were consistent across the five patients tested (Fig. S1 E). The cut-off points were then selected based on the relative density ranges of each tissue region. Relative to the maximum cell density in each patient, the healthy region was defined by densities between 0 and 25%, the consolidated region between 25 and 50%, and the aggregate region between 50 and 100%. To visualize the regions defined by cellular density on tissue images, the Density Heatmap tool in HALO was applied to map density across the entire tissue section, and the annotation tool was used to define the regions for export.

To refine the lesion identification, kernel density analysis was further performed on cells that were stained positively for at least one of four immune cell markers (CD20, CD68, CD4, or CD8) in R. 3D density projection was again performed with persp function, and areas between 20 and 100% of the maximum cell density were considered as diseased tissue areas. Lesions were identified using HALO with the density heatmap function and lesion boundaries were drawn using the annotation tool. Cell segmentation was performed in batch on all lesions and object data was exported to R.

Necrotizing lesions in IF images were primarily delineated from non-necrotizing lesions based on the presence of necrosis on matching sections stained with H&E. The presence of a central DAPI-negative area with autofluorescent necrotic

debris was also used to confirm necrotizing lesions in IF images.

Lesion clustering analysis based on intra-lesion immune cell density

The area of individual lesions was determined using HALO summary data in R. The relative abundance of individual immune cell populations in each lesion was expressed as immune cells per square millimeter of lesion area. Lesion clustering analysis was performed using PCA with a density of CD8⁺, CD20⁺, CD4⁺, and CD68⁺ cells used as parameters. PCA was performed in R with the “prcomp” function with “scale = True”. PCA results were visualized using the factoextra package (Kassambara and Mundt, 2021) with functions “fviz_pca_ind” and “fviz_pca_var”.

Total cell central preference index, immune cell central preference index, and necrotic distance index calculations

The Infiltration Analysis tool in HALO was applied to each lesion to measure the distance of each cell from the lesion border, with the store object data set as true to save individual cell data. Data were imported into R and cell distance information was matched to previous cell data by cell ID. To determine the central preference index of all DAPI⁺ cells (tCPI), the median cell distance from the border was identified with the median function in R. The area of lesion encompassing the inner/outer 50% of cells was then calculated in HALO using the infiltration tool. The tCPI was calculated as:

$$\text{total cell central preference index} = \frac{\text{Area}^{\text{Outer 50\% of cells}}}{\text{Area}^{\text{Total lesion}}}$$

For immune cell preference index (immCPI) determination, cell distance measurements from lesion borders used in tCPI calculation were applied to cells based on their immune cell lineage identity. The relative distance of each marker from the lesion border was calculated as follows:

$$\text{immune cell central preference index} = \frac{\text{Mean Distance}^{\text{immune cell of interest}}}{\text{Mean Distance}^{\text{All cells}}}$$

The relative distance of each marker from the necrotizing interface was calculated as follows:

$$\text{Necrotic distance index} = \frac{\text{Mean Distance}^{\text{Cell of interest}}}{\text{Mean Distance}^{\text{All cells}}}$$

Definition of lesion types

When dividing lesions into four types, the x-axis cut-off was set at zero as this was the mean value of the PCI axis and divided the scores evenly. Splitting at zero also assists in dividing the lesions with high and low B cell density (Fig. 2 C, top right panel). The y-axis cut-off was set at 0.5 as this was the point about which the distribution of cells changed between more centrally distributed and more peripherally distributed.

Definition of M.tb clusters

M.tb and/or its products were identified based on anti-PPD staining and distinct clusters were delineated visually.

Lesion neighborhood and trajectory analysis

The minimum distance between each non-necrotizing lesion to a necrotizing lesion was calculated in R using the “pointDistance” function from the raster package (Hijmans and Etten, 2012). All cells from one lesion were measured with regard to another, and the “minimum” function applied to the result identified the minimum distance between the two lesions.

Data from immune cell densities, tCPI, and immCPI were collated into a matrix, and functions from the SCORPIUS package (Cannoodt et al., 2016 Preprint) were used to produce the trajectory plot and trajectory heatmap.

Statistical analysis

All statistical analyses were performed in GraphPad Prism 9.1.2. Single comparisons were performed using a Mann–Witney test. Multiple comparisons were performed using a Kruskal–Wallis test with Dunn’s multiple comparisons test. Paired single comparisons were performed using a Wilcoxon matched-pairs signed rank test. A P value <0.05 was considered statistically significant for all tests. All plots were generated using GraphPad Prism or R.

Online supplemental material

Fig. S1 shows each patient sample and pathological features. Fig. S2 characterizes the four lesion types identified in the study. Table S1 contains clinical information for all patients included in the study.

Data availability

The data underlying Figs. 1, 2, 3, 4, and 5 are available in the published article and its online supplemental material.

Acknowledgments

We acknowledge Clifton Barry III and Laura Via for their thoughtful discussion. We also thank Dr. Angela Ferguson for her advice on tissue staining.

This work was supported by US National Institutes of Health (grant U01AI166309) and the Natural Science Foundation of China (grant 91942315). A.J. Sawyer and J. Edwards were supported by Australian Postgraduate Awards.

Author contributions: Conceptualization, A.J. Sawyer and C.G. Feng; Investigation, A.J. Sawyer, J. Edwards, and T. Fielder; Data analysis: A.J. Sawyer, E. Patrick, T. Fielder, and C.G. Feng; Resources, J.S. Wilmott, Q. Yang, D.L. Barber, J.D. Ernst, W.J. Britton, U. Palendira, and X. Chen; Writing—Original Draft, A.J. Sawyer and C.G. Feng; Writing—Review & Editing, All authors; Funding Acquisition, C.G. Feng, X. Chen, J.D. Ernst, D.L. Barber, and E. Patrick; Supervision, C.G. Feng.

Disclosures: J. Edwards reported being currently employed by Bristol Myers Squibb, but was not employed at the time the data was generated and analyzed. No other disclosures were reported.

Submitted: 15 August 2022

Revised: 7 January 2023

Accepted: 28 February 2023

References

- Abengozar-Muela, M., M.V. Esparza, D. Garcia-Ros, C.E. Vásquez, J.I. Echeveste, M.A. Idoate, M.D. Lozano, I. Melero, and C.E. de Andrea. 2020. Diverse immune environments in human lung tuberculosis granulomas assessed by quantitative multiplexed immunofluorescence. *Mod. Pathol.* 33:2507–2519. <https://doi.org/10.1038/s41379-020-0600-6>
- Basaraba, R.J., and R.L. Hunter. 2017. Pathology of tuberculosis: How the pathology of human tuberculosis informs and directs animal models. *Microbiol. Spectr.* 5:5. <https://doi.org/10.1128/microbiolspec.TB2017-0029-2016>
- Barry, C.E., III, H.I. Boshoff, V. Dartois, T. Dick, S. Ehrh, J. Flynn, D. Schnappinger, R.J. Wilkinson, and D. Young. 2009. The spectrum of latent tuberculosis: Rethinking the biology and intervention strategies. *Nat. Rev. Microbiol.* 7:845–855. <https://doi.org/10.1038/nrmicro2236>
- Cadena, A.M., S.M. Fortune, and J.L. Flynn. 2017. Heterogeneity in tuberculosis. *Nat. Rev. Immunol.* 17:691–702. <https://doi.org/10.1038/nri.2017.69>
- Cannoodt, R., W. Saelens, D. Sichiens, S. Tavernier, S. Janssens, M. Guillemins, B. Lambrecht, K.D. Preter, and Y. Saeys. 2016. SCORPIUS improves trajectory inference and identifies novel modules in dendritic cell development. *bioRxiv*. (Preprint posted October 07, 2016). <https://doi.org/10.1101/079509>
- Carow, B., T. Hauling, X. Qian, I. Kramnik, M. Nilsson, and M.E. Rottenberg. 2019. Spatial and temporal localization of immune transcripts defines hallmarks and diversity in the tuberculosis granuloma. *Nat. Commun.* 10:1823. <https://doi.org/10.1038/s41467-019-09816-4>
- Cohen, S.B., B.H. Gern, and K.B. Urdahl. 2022. The tuberculous granuloma and preexisting immunity. *Annu. Rev. Immunol.* 40:589–614. <https://doi.org/10.1146/annurev-immunol-093019-125148>
- Cronan, M.R., E.J. Hughes, W.J. Brewer, G. Viswanathan, E.G. Hunt, B. Singh, S. Mehra, S.H. Oehlers, S.G. Gregory, D. Kaushal, and D.M. Tobin. 2021. A non-canonical type 2 immune response coordinates tuberculous granuloma formation and epithelialization. *Cell.* 184:1757–1774.e14. <https://doi.org/10.1016/j.cell.2021.02.046>
- Garnier, S., N. Ross, B. Rudis, M. Sciaini, A.P. Camargo, and C. Scherer. 2021. Viridis: Colorblind-friendly color maps for R. <https://sjmgarnier.github.io/viridis/>.
- Gideon, H.P., T.K. Hughes, C.N. Tzouanas, M.H. Wadsworth II, A.A. Tu, T.M. Gierahn, J.M. Peters, F.F. Hopkins, J.R. Wei, C. Kummerlowe, et al. 2022. Multimodal profiling of lung granulomas in macaques reveals cellular correlates of tuberculosis control. *Immunity.* 55:827–846.e10. <https://doi.org/10.1016/j.immuni.2022.04.004>
- Hartmann, F.J., and S.C. Bendall. 2020. Immune monitoring using mass cytometry and related high-dimensional imaging approaches. *Nat. Rev. Rheumatol.* 16:87–99. <https://doi.org/10.1038/s41584-019-0338-z>
- Hijmans, R.J., and J.V. Etten. 2012. Raster: Geographic analysis and modeling with raster data. <http://CRAN.R-project.org/package=raster>.
- Hunter, R.L. 2011. Pathology of post primary tuberculosis of the lung: An illustrated critical review. *Tuberculosis.* 91:497–509. <https://doi.org/10.1016/j.tube.2011.03.007>
- Hunter, R.L. 2016. Tuberculosis as a three-act play: A new paradigm for the pathogenesis of pulmonary tuberculosis. *Tuberculosis.* 97:8–17. <https://doi.org/10.1016/j.tube.2015.11.010>
- Hunter, R.L., J.K. Actor, S.A. Hwang, V. Karev, and C. Jagannath. 2014. Pathogenesis of post primary tuberculosis: Immunity and hypersensitivity in the development of cavities. *Ann. Clin. Lab. Sci.* 44:365–387.
- Libardo, M.D.J., H.I. Boshoff, and C.E. Barry III. 2018. The present state of the tuberculosis drug development pipeline. *Curr. Opin. Pharmacol.* 42: 81–94. <https://doi.org/10.1016/j.coph.2018.08.001>
- Kassambara, A. and F. Mundt. 2021. Factoextra: Extract and visualize the results of multivariate data analyses. <https://CRAN.R-project.org/package=factoextra>.
- Kim, M.J., H.C. Wainwright, M. Locketz, L.G. Bekker, G.B. Walther, C. Ditrach, A. Visser, W. Wang, F.F. Hsu, U. Wiehart, et al. 2010. Caseation of human tuberculosis granulomas correlates with elevated host lipid metabolism. *EMBO Mol. Med.* 2:258–274. <https://doi.org/10.1002/emmm.201000079>
- Lin, P.L., and J.L. Flynn. 2018. The end of the binary era: Revisiting the spectrum of tuberculosis. *J. Immunol.* 201:2541–2548. <https://doi.org/10.4049/jimmunol.1800993>
- Lin, P.L., C.B. Ford, M.T. Coleman, A.J. Myers, R. Gawande, T. Ioerger, J. Sacchetti, S.M. Fortune, and J.L. Flynn. 2014. Sterilization of granulomas is common in active and latent tuberculosis despite within-host variability in bacterial killing. *Nat. Med.* 20:75–79. <https://doi.org/10.1038/nm.3412>

- Ma, F., T.K. Hughes, R.M.B. Teles, P.R. Andrade, B.J. de Andrade Silva, O. Plazyo, L.C. Tsoi, T. Do, M.H. Wadsworth II, A. Oulee, et al. 2021. The cellular architecture of the antimicrobial response network in human leprosy granulomas. *Nat. Immunol.* 22:839–850. <https://doi.org/10.1038/s41590-021-00956-8>
- Marakalala, M.J., R.M. Raju, K. Sharma, Y.J. Zhang, E.A. Eugenin, B. Prideaux, I.B. Daudelin, P.Y. Chen, M.G. Booty, J.H. Kim, et al. 2016. Inflammatory signaling in human tuberculosis granulomas is spatially organized. *Nat. Med.* 22:531–538. <https://doi.org/10.1038/nm.4073>
- Martin, C.J., A.M. Cadena, V.W. Leung, P.L. Lin, P. Maiello, N. Hicks, M.R. Chase, J.L. Flynn, and S.M. Fortune. 2017. Digitally barcoding *Mycobacterium tuberculosis* reveals in vivo infection dynamics in the macaque model of tuberculosis. *MBio.* 8:e00312–e00317. <https://doi.org/10.1128/mBio.00312-17>
- Mattila, J.T., W. Beaino, P. Maiello, M.T. Coleman, A.G. White, C.A. Scanga, J.L. Flynn, and C.J. Anderson. 2017. Positron emission tomography imaging of macaques with tuberculosis identifies temporal changes in granuloma glucose metabolism and integrin $\alpha 4\beta 1$ -expressing immune cells. *J. Immunol.* 199:806–815. <https://doi.org/10.4049/jimmunol.1700231>
- McCaffrey, E.F., M. Donato, L. Keren, Z. Chen, A. Delmastro, M.B. Fitzpatrick, S. Gupta, N.F. Greenwald, A. Baranski, W. Graf, et al. 2022. The immunoregulatory landscape of human tuberculosis granulomas. *Nat. Immunol.* 23:318–329. <https://doi.org/10.1038/s41590-021-01121-x>
- Medlar, E.M. 1948. The pathogenesis of minimal pulmonary tuberculosis; a study of 1,225 necropsies in cases of sudden and unexpected death. *Am. Rev. Tuberc.* 58:583–611. <https://doi.org/10.1164/art.1948.58.6.583>
- Medlar, E.M. 1955. The behavior of pulmonary tuberculous lesions; a pathological study. *Am. Rev. Tuberc.* 71:1–244.
- Orme, I.M., R.T. Robinson, and A.M. Cooper. 2015. The balance between protective and pathogenic immune responses in the TB-infected lung. *Nat. Immunol.* 16:57–63. <https://doi.org/10.1038/ni.3048>
- O'Garra, A., P.S. Redford, F.W. McNab, C.I. Bloom, R.J. Wilkinson, and M.P.R. Berry. 2013. The immune response in tuberculosis. *Annu. Rev. Immunol.* 31:475–527. <https://doi.org/10.1146/annurev-immunol-032712-095939>
- Pagán, A.J., and L. Ramakrishnan. 2018. The formation and function of granulomas. *Annu. Rev. Immunol.* 36:639–665. <https://doi.org/10.1146/annurev-immunol-032712-100022>
- R Core Team. 2021. R: A language and environment for statistical computing. <https://www.R-project.org/>.
- Ramakrishnan, L. 2012. Revisiting the role of the granuloma in tuberculosis. *Nat. Rev. Immunol.* 12:352–366. <https://doi.org/10.1038/nri3211>
- Slight, S.R., J. Rangel-Moreno, R. Gopal, Y. Lin, B.A. Fallert Junecko, S. Mehra, M. Selman, E. Becerril-Villanueva, J. Baquera-Heredia, L. Pavon, et al. 2013. CXCR5⁺ T helper cells mediate protective immunity against tuberculosis. *J. Clin. Invest.* 123:712–726. <https://doi.org/10.1172/JCI65728>
- Subbian, S., L. Tsenova, M.J. Kim, H.C. Wainwright, A. Visser, N. Bandyopadhyay, J.S. Bader, P.C. Karakousis, G.B. Murrmann, L.G. Bekker, et al. 2015. Lesion-specific immune response in granulomas of patients with pulmonary tuberculosis: A pilot study. *PLoS One.* 10:e0132249. <https://doi.org/10.1371/journal.pone.0132249>
- Tan, W.C.C., S.N. Nerurkar, H.Y. Cai, H.H.M. Ng, D. Wu, Y.T.F. Wee, J.C.T. Lim, J. Yeong, and T.K.H. Lim. 2020. Overview of multiplex immunohistochemistry/immunofluorescence techniques in the era of cancer immunotherapy. *Cancer Commun.* 40:135–153. <https://doi.org/10.1002/cac2.12023>
- Tsai, M.C., S. Chakravarty, G. Zhu, J. Xu, K. Tanaka, C. Koch, J. Tufariello, J. Flynn, and J. Chan. 2006. Characterization of the tuberculous granuloma in murine and human lungs: Cellular composition and relative tissue oxygen tension. *Cell. Microbiol.* 8:218–232. <https://doi.org/10.1111/j.1462-5822.2005.00612.x>
- Ulrichs, T., G.A. Kosmiadi, V. Trusov, S. Jörg, L. Pradl, M. Titukhina, V. Mishenko, N. Gushina, and S.H.E. Kaufmann. 2004. Human tuberculous granulomas induce peripheral lymphoid follicle-like structures to orchestrate local host defence in the lung. *J. Pathol.* 204:217–228. <https://doi.org/10.1002/path.1628>
- Urbanowski, M.E., A.A. Ordonez, C.A. Ruiz-Bedoya, S.K. Jain, and W.R. Bishai. 2020. Cavitory tuberculosis: The gateway of disease transmission. *Lancet Infect. Dis.* 20:e117–e128. [https://doi.org/10.1016/S1473-3099\(20\)30148-1](https://doi.org/10.1016/S1473-3099(20)30148-1)
- Venables, W.N., and B.D. Ripley. 2002. *Modern Applied Statistics with S*. Springer, New York.
- Wells, G., J.N. Glasgow, K. Nargan, K. Lumamba, R. Madansein, K. Maharaj, R.L. Hunter, T. Naidoo, L. Coetzer, S. le Roux, et al. 2021. Micro-computed tomography analysis of the human tuberculous lung reveals remarkable heterogeneity in three-dimensional granuloma morphology. *Am. J. Respir. Crit. Care Med.* 204:583–595. <https://doi.org/10.1164/rccm.202101-00320C>
- Welsh, K.J., S.A. Risin, J.K. Actor, and R.L. Hunter. 2011. Immunopathology of postprimary tuberculosis: Increased T-regulatory cells and DEC-205-positive foamy macrophages in cavitory lesions. *Clin. Dev. Immunol.* 2011:307631. <https://doi.org/10.1155/2011/307631>
- Williams, A., and I.M. Orme. 2016. Animal models of tuberculosis: An overview. *Microbiol. Spectr.* 4:4. <https://doi.org/10.1128/microbiolspec.TB2B2-0004-2015>
- World Health Organization. 2021. Global tuberculosis report 2021. <https://www.who.int/publications/i/item/9789240037021>

Supplemental material

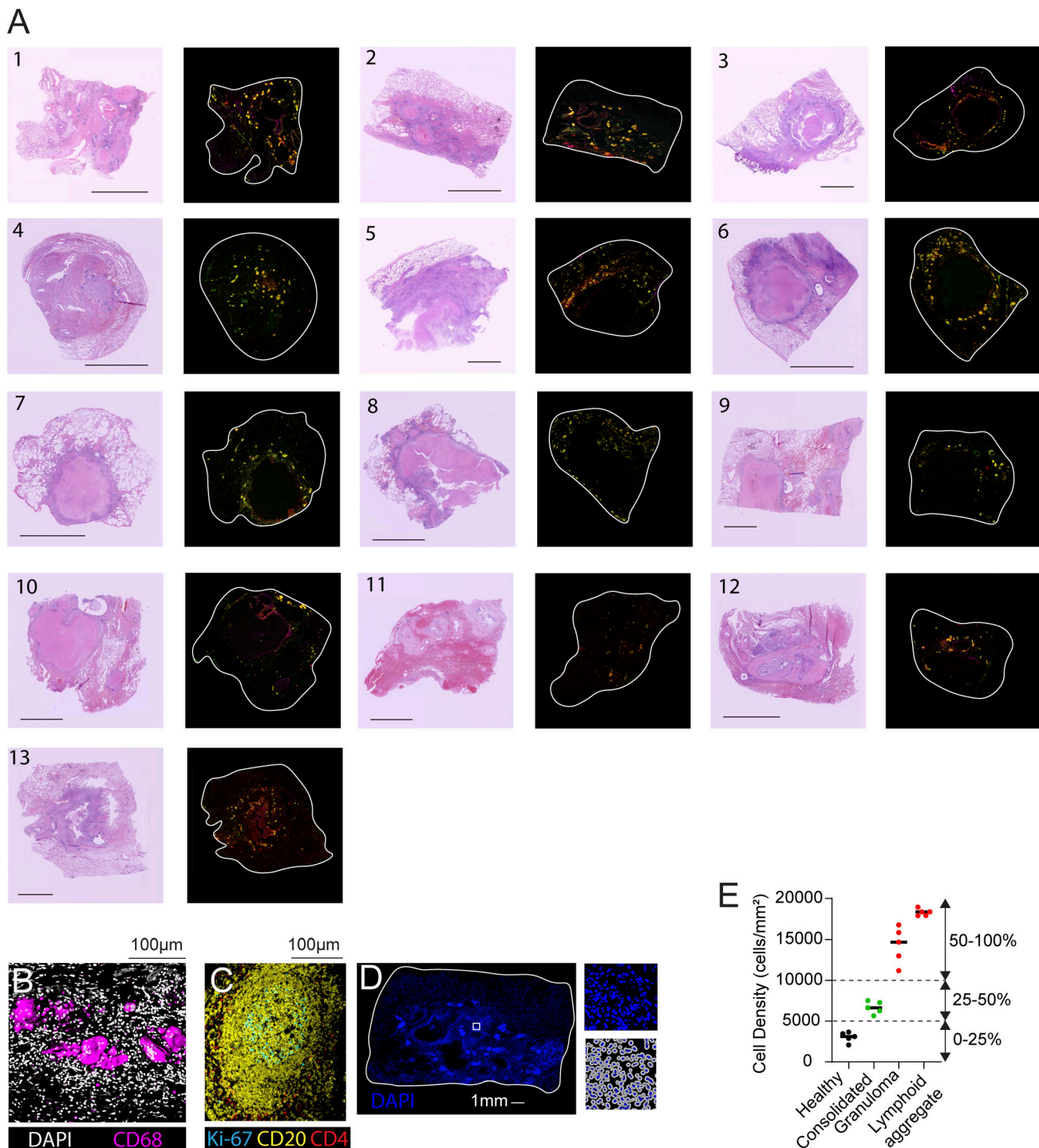


Figure S1. **Tissue landscape of the *M.tb*-infected lung.** (A) H&E staining of lung tissue samples used in this study with matching multiplex IF staining with CD20, CD4, CD8, and CD68. Scale bars represent 5 mm. (B) Representative image of giant cells identified based on morphology and CD68 and DAPI staining. (C) Representative multiplex staining with CD20, CD4, and Ki-67 showing a Germinal center-like structure. (D) The same composite image of TB lung section as in Fig. 1A stained with DAPI, with a representative view of segmented cells shown. (E) Cell density within tissue regions defined pathologically on H&E-stained tissue ($n = 5$). Dotted lines indicate density thresholds selected for tissue classification in Fig. 1, F and G.

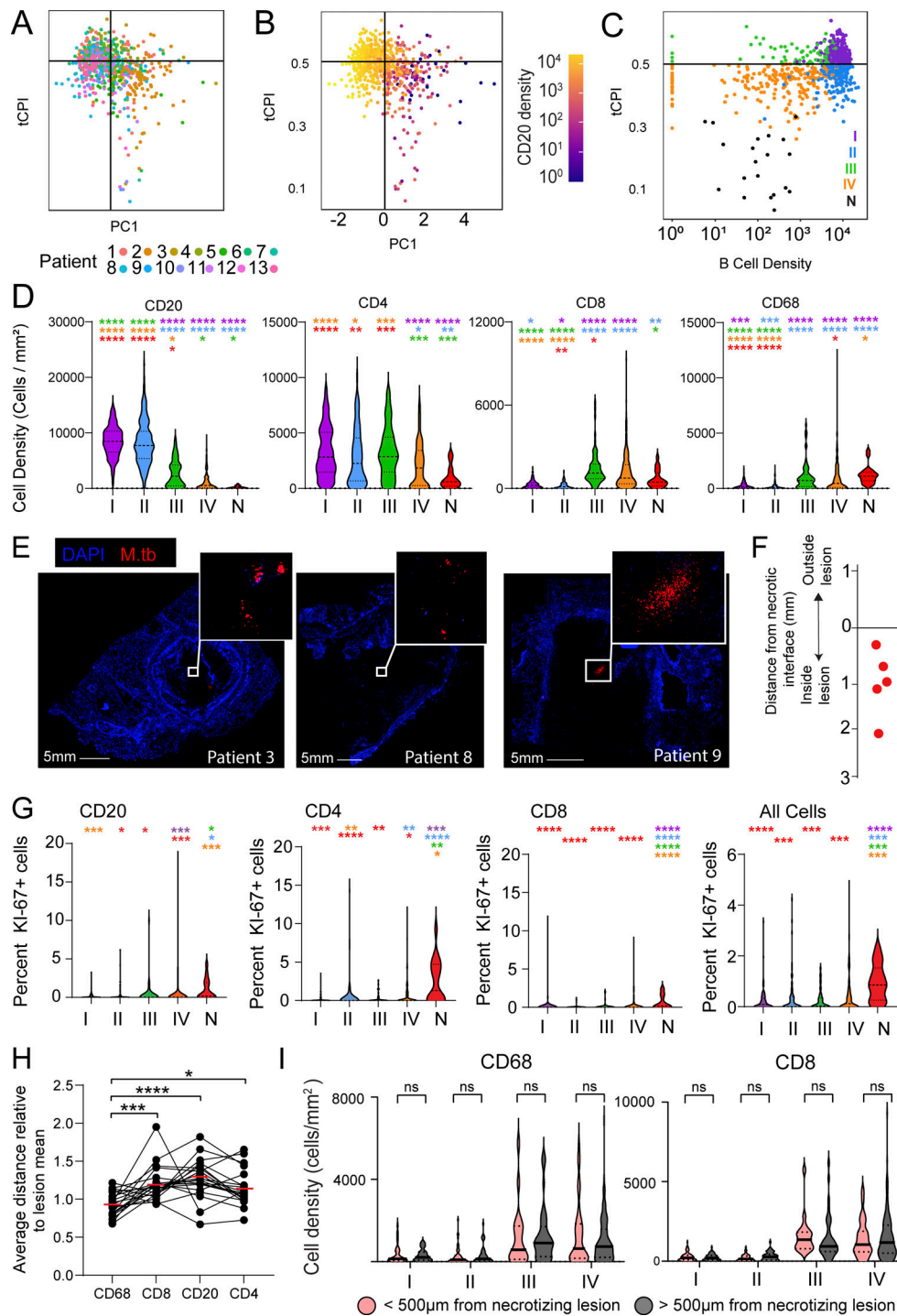


Figure S2. **Lesion cellular features in the lungs of TB patients.** (A) Comparison of PC1 against tCPI from Fig. 3 E colored according to patient. (B) Comparison of PC1 against tCPI from Fig. 3 E colored according to the density of CD20⁺ B cells. (C) Comparison of CD20⁺ B cell density against tCPI. Each symbol represents an individual lesion, and lesions are colored according to type as Fig. 3 E. A value of 1 was added to the density of all lesions to allow lesions with no CD20⁺ B cells to be displayed on the log scale. (D) Density of major immune populations according to lesion type. Solid lines indicate the group median and dotted lines indicate interquartile range. (E) IF images stained for M.tb and DAPI with magnified views of the indicated boxed areas. Middle image represents the same tissue section as Fig. 4 E. (F) Distance of M.tb clusters from the necrotic interface in necrotizing lesions. M.tb was not identified in non-necrotizing regions. Each symbol represents a well-formed M.tb cluster (total five identified in the three lesions shown in A). (G) Proportion of major cell populations positive for Ki-67. Solid lines indicate the group median and dotted lines indicate interquartile range. (H) Necrotizing cell index of major immune populations. Each symbol represents an individual necrotizing lesion and lines track data from the same lesion. Solid red lines represent the group median. (I) Density of CD8⁺ and CD68⁺ cells in lesions located greater or less than 500 µm from necrotizing lesions. Solid lines indicate the group median and dotted lines indicate interquartile range. The level of statistical significance in I is determined using a Mann-Whitney test, and a P value <0.05 was considered statistically significant. **P < 0.01; ***P < 0.001. The level of statistical significance in D, G, and H is determined using a Kruskal-Wallis test with Dunn's multiple comparisons test, and an adjusted P value <0.05 was considered statistically significant. *P < 0.05; **P < 0.01; ***P < 0.001; ****P < 0.0001.

Provided online is Table S1. Table S1 shows clinical information for all patients included in the study.